Implementation of complex signal processing algorithms for position-sensitive microcalorimeters

Stephen J. Smith*

NASA Goddard Space Flight Center, Greenbelt, MD 20771, USA.

Abstract: We have recently reported on a theoretical digital signal-processing algorithm for improved energy and position resolution in position-sensitive, transition-edge sensor (PoST) X-ray detectors [Smith et al., Nucl. Instr and Meth. A 556 (2006) 237]. PoST's consists of one or more transition-edge sensors (TES's) on a large continuous or pixellated X-ray absorber and are under development as an alternative to arrays of single pixel TES's. PoST's provide a means to increase the field-of-view for the fewest number of read-out channels. In this contribution we extend the theoretical correlated energy position optimal filter (CEPOF) algorithm (originally developed for 2-TES continuous absorber PoST's) to investigate the practical implementation on multi-pixel single TES PoST's or Hydras. We use numerically simulated data for a nine absorber device, which includes realistic detector noise, to demonstrate an iterative scheme that enables convergence on the correct photon absorption position and energy without any a priori assumptions. The position sensitivity of the CEPOF implemented on simulated data agrees very well with the theoretically predicted resolution. We discuss practical issues such as the impact of random arrival phase of the measured data on the performance of the CEPOF. The CEPOF algorithm demonstrates that full-width-at-half-maximum energy resolution of < 8 eV coupled with position-sensitivity down to a few 100 eV should be achievable for a fully optimized device.

Keywords: Transition-edge sensor; position-sensitive X-ray detector; microcalorimeter; International X-ray Observatory; correlated energy position optimal filter.

PACS: 07.85.Fv; 95.55.Ka; 95.75.Pq

* Corresponding Author. email: stephen.j.smith@nasa.gov; tel.:1-301-286-3719; fax: 1-301-286-1684.

1. Introduction

At NASA Goddard Space Flight Center, we are developing microcalorimeters such as transition-edge sensors (TES's) [1] and metallic magnetic calorimeters (MMC's) [2] for X-ray astronomy missions such as the International X-ray Observatory (IXO), jointly under study by NASA and ESA. IXO is a merger of NASA's Constellation-X [3] and ESA's XEUS [4] mission concepts. Beyond IXO, this development is targeted at NASA's Generation-X 'vision mission' [5]. Arrays of single pixel TES's offer impressive full-width-at-half-maximum (FWHM) energy resolution of $\Delta E \sim 2$-3 eV in the soft X-ray energy range coupled with count-rates that can accommodate up to 100's per pixel per second [6-8]. Alternatives to single pixel arrays are position-sensitive TES's (PoST's) [9]. PoST's consist of either a single large absorber or a series of segmented absorbers, which are thermally coupled to one or more read-out sensor [10-13]. Heat diffusion between the absorber(s) and the TES's gives rise to position dependence of the pulse shapes and enables position discrimination. Such devices are aimed at reducing the number of read-out channels for a given focal plane area at some expense in energy resolution and count-rate capability.

We are currently pursuing single-channel PoST's, commonly referred to as Hydras, which consist of multiple absorber elements each with a different thermal coupling to a single TES readout channel. Results from first generation 4-pixel Hydras have demonstrated FWHM energy resolution of between 5-6 eV at an energy of 5.9 keV for devices with a 250 μm pixel pitch [13-15]. We are extending this approach to incorporate more absorber elements, enabling further increases in the field-of-view for missions such as IXO, and further, to investigate alternative MMC Hydra designs.

The ability to differentiate between different pulse shapes scales with the photon energy E [16]. For a segmented absorber PoST, such as the Hydra, the pulse shapes are quantized and the position resolution (Δx) is constrained by the pixel size. Below some threshold energy the signal-to-noise will be degraded such that it is not possible to distinguish between different shapes of pulse and position sensitivity will be lost. For a continuous absorber device it follows that $\Delta x \propto 1/E$. Thus continuous PoST's can potentially achieve very high position resolution. However in the continuous devices, the position x and energy E are intrinsically correlated such that an error in the x (due to noise) will propagate into an error in E. Depending upon the specific device design, this can result in a significant

degradation in ΔE. The signal processing analysis is typically more computationally intense for the continuous absorber case since there is a continuous population of different pulse shapes, as opposed to a discrete set corresponding to each element of a segmented absorber. The energy of the photon is found using a digital optimal filter [17], optimised for a specific pulse shape. Consequently a much larger number of template filters will be required (of the order $L/\Delta x$, where L is the linear dimension of the detector), otherwise the filters will not be well matched to the pulse shapes and some loss in resolution will result.

We are developing complex signal-processing algorithms for position-sensitive microcalorimeters [15,16,18]. In ref. [16] we reported a theoretical signal-processing algorithm for simultaneous determination of the energy and position in one-dimensional (continuous absorber) 2-TES PoST's. In this contribution we adapt this correlated energy-position optimal filter (CEPOF) algorithm to investigate segmented absorber devices such as the Hydra, which we are currently developing for IXO. We use numerically simulated pulses (for a 9-pixel Hydra), which include realistic detector noise to demonstrate an iterative implementation method, which converges on the correct photon position and energy without any a priori assumptions.

2. Hydra numerical model

To simulate realistic pulse and noise data we use the fourth order Runge-Kutta [19] technique to integrate a system of ordinary non-linear differential equations that describes the Hydra. For this study we assume a 9-pixel Hydra, which is an alternative to the 4-pixel devices already experimentally characterised. Fig. 1 shows a schematic diagram of the 9-pixel Hydra concept. Each Hydra absorber is modelled as a single heat capacity C coupled to a TES via a link conductance G_L. We use typical design parameters from the experimental characterisation of the 4-pixel designs. Table 1 lists the design parameters used in this study. We assume a linear current and temperature dependent resistive transition of the form

$$R(T,I) = R_0 + \alpha \frac{R_0}{T_0} \Delta T + \beta \frac{R_0}{I_0} \Delta I, \qquad (1)$$

where R_0, T_0 and I_0 are the detector resistance, temperature and current at the quiescent operating point and α and β are the unit-less TES resistance and current sensitivities respectively. Over typical resistance excursions due to 5.9 keV photons, such a transition shape is found to describe the experimentally measured pulse shapes accurately. To incorporate realistic detector noise we use a random number generator with Gaussian distribution, which is added to the input of the model at every time step. For the TES near equilibrium, non-linear Johnson noise [20] we set the variance of our Gaussian noise to $(4k_bT_0R_0\Delta B(1+2\beta))^{1/2}$ (in units of volts) where k_b is the Boltzmann constant and ΔB is the bandwidth of the noise, which in the context of our numerical model is equivalent to $1/(2\Delta t)$, where Δt is the integration step size. We also include the Johnson from the TES bias circuit, which has the same form except it is in equilibrium hence we drop the β dependence. For the thermal fluctuation (phonon) noise between the different detector heat capacities as well as the detector and the heat sink, we have $(4k_bT_0^2G\gamma\Delta B)^{1/2}$ (in units of watts), where G is the thermal conductance between the relevant detector elements and γ is a unit-less constant which describes the temperature gradient across the conductance link [21]. It is ~ 0.5 for the thermal fluctuation noise between the TES and heat sink and is ~ 1 for the internal thermal links which are approximately isothermal. In our 4-pixel Hydras we observed an excess in the low frequency noise of approximately 1.2 times the level of the phonon noise to the heat sink [14], which we also include in this model. A white readout noise equivalent to 5 pA/$\sqrt{\text{Hz}}$ on the TES input is also assumed. This model intrinsically includes non-linearity of the pulse shape as well as any associated non-stationary noise. Fig. 2a shows a plot of the simulated pulse shapes for the 9-pixel Hydra with design parameters as listed in Table 1, the noise terms are set to zero. The internal thermal conductances are chosen to give approximately equal spacing between the pulse shapes. Fig. 2b then shows the frequency domain plot of the same pulse shapes as well as the noise power spectral density averaged over 400 simulated noise traces. Both the pulses and the noise spectral density agree well with that predicted from linear small signal responsivity models (such as that described in refs. [14,22]) using the same device parameters.

3. Correlated energy-position optimal filter (CEPOF) algorithm

The CEPOF algorithm is an adaptation of the standard digital optimal filter for determining photon energy in single pixel calorimeters [17]. In a PoST we want to solve for both the energy and the position simultaneously. When a photon is absorbed at position x_γ on a one-dimensional absorber, the measured data D can be modelled as a (first

order) Taylor expansion around some reference position x such that $D = H(S + (x_\gamma - x)S')$, where S is the signal responsivity, $S' = dS/dx$ is derivative of S with x and H is a scalar representing the photon energy. Thus, to construct our CEPOF we minimise the difference between the measured data and our modelled pulse. In one-dimension, with n TES readout channels, the χ^2 condition to minimise is [16]:

$$\chi^2 = \sum \left[D - H\left(S + \delta x S'\right)\right]^{*T} W \left[D - H\left(S + \delta x S'\right)\right], \tag{1}$$

where D, S are S' are n element vectors containing the data, responsivity and derivative of the responsivity respectively for each TES. W is the weight matrix and is the inverse of the $n \times n$ variance-covariance matrix, which describes the detector noise. Eq. 1 is easily adapted for the Hydra case, which consists of a singe TES ($n = 1$) connected to a series of m absorber elements:

$$\chi^2 = \sum \frac{\left(D - H\left(S_i + \delta i S_i'\right)\right)^2}{\left\langle |N|^2 \right\rangle}, \tag{2}$$

here, N^2 is the measured power spectral density of the noise. Even though they may not be physically positioned in any particular order, for the purpose of this algorithm we can reference the absorbers in order of most similar pulse shapes from $i = 1 \ldots m$. Thus we replace the continuous position variable x with an integer position i. Then, S_i is calculated for each absorber i and their derivatives are evaluated between sequentially ordered absorbers such that $S'_i = dS_i/di$. δi is then simply $(i_\gamma - i)$. As described in [16], we can minimise Eq. 2 with respect to δi and H, which leads to a pair of simultaneous equations in $H\delta i$ and H which have the solution:

$$\begin{pmatrix} H \\ H\delta i \end{pmatrix} = \left[\sum F_i S_i \sum F_i' S_i' - \left(\sum F_i' S_i\right)^2\right]^{-1} \begin{pmatrix} \sum F_i' S_i' & -\sum F_i' S_i \\ -\sum F_i' S_i & \sum F_i S_i \end{pmatrix} \begin{pmatrix} \sum F_i D \\ \sum F_i' D \end{pmatrix}. \tag{3a}$$

Collecting normalisation terms into the constants k_{i1}, k_{i2} and k_{i3} we can write

$$H = k_{i1}\sum F_i D_i + k_{i2}\sum F_i' D_i \qquad (3b)$$

and

$$H\delta i = k_{i2}\sum F_i D_i + k_{i3}\sum F_i' D_i . \qquad (3c)$$

For our Hydra we have m template optimal filters of the form $F_i = S_i^*/N^2$. F_i' is then the derivative of the filter with respect to position i. Thus if we apply a filter corresponding to an absorber i the CEPOF will give a self consistent estimate of both the energy H and the relative position δi from the assumed starting position i. If the first order derivatives exactly match the variation in pulse shape across all absorbers then this will give the correct energy and position. However, in reality the first order terms may only be accurate close to the true absorber position. Consequently some iteration may be required to converge on the correct pixel. Fig. 3a shows, for the Hydra case outlined in Section 2, the calculated value of δi (using Eq. 3) for each pixel i, for a single 100 eV X-ray with no noise, absorbed in pixel $i = 5$. The filters and derivatives are all calculated using the 100 eV template pulse and the average of 400 noise traces. The presence of noise and error in the derivative function at larger δi means that δi may not be an exact integer value. Thus to converge on a solution we must round δi to the nearest integer value. In this example, the maximum number of iterations after the initial estimate required to converge to $\delta i = 0$ is 3, though the typical result is only 1 iteration. Fig. 3b shows the calculated value of the photon energy H for the same test case. Also shown in this plot is the effect of dropping the correlation term in Eq. 3 $F'S$ ($k_i2 = 0$) then our energy calculation becomes independent of position and H_i-E (for $i \neq i_\gamma$) becomes significantly larger.

4. Energy resolution and position sensitivity

Assuming we have converged to the correct pixel ($\delta i = 0$), the theoretical root-mean-squared (rms) energy resolution and position resolution are found from the variance on H and $H\delta i$ [16,23]:

$$\Delta i = \frac{\left[\sum F_i S_i\right]^{1/2}}{2E\left[\sum F_i S_i \sum F_i' S_i' - \left(\sum F_i' S_i\right)^2\right]^{1/2}}, \tag{4a}$$

and

$$\Delta E = \frac{\left[\sum F_i' S_i'\right]^{1/2}}{2\left[\sum F_i S_i \sum F_i' S_i' - \left(\sum F_i' S_i\right)^2\right]^{1/2}}. \tag{4b}$$

For our segmented absorber example, the units of Δi are in pixel number or i. Assuming a Gaussian distribution of δi around $\delta i = 0$, we can convert Δi into a probability P_i that a photon will be assigned to the correct pixel or its neighbouring pixels. The probability of an event with $|\delta i| \geq x$ can be found from the complementary Gaussian error function, *erfc*,

$$P_i(xa) = A\frac{2}{\sqrt{\pi}}\int_{xa}^{\infty} e^{-u^2}\,du = A\,erfc(xa), \tag{5a}$$

where,

$$a = \frac{1}{2\sqrt{2}}\frac{1}{\Delta i}. \tag{5b}$$

For the end pixels ($i = 0$ and $i = m$) we set $A = 0.5$ and for all other pixels ($i = 1 \ldots m\text{-}1$), $A = 1$. For $x = 1$, Eq. 5 gives the probability that the photon will be assigned to the incorrect pixel ($i \neq i_\gamma$), for $x = 3$ this is the probability that the photon will have an assignment error of greater than 1 pixel either side of i_γ. Fig. 4 shows the calculated probability of an incorrect pixel assignment ($x = 1$) using Eq. 5 for all the absorber pixels with a photon energy of $E = 50$ eV. Also shown in this plot is the actual error in a sample of 100 simulated photons in which we calculate the pixel

assignment using Eq. 3. To demonstrate the intrinsic position error at $\delta i = 0$ we assume a starting position of $i = i_\gamma$ (circle symbols). Both the theoretically calculated and the actual position error show on average very good agreement across all pixels. In a real detector where we have no a priori information about the event, we must start at some fixed pixel, such as the center pixel $i = 5$ for example and allow the CEPOF algorithm to converge to a solution. Depending upon the level of noise and the accuracy of the derivative functions this can result in a convergence error due to a local minimum in δi. This data is also shown in Fig. 4 (star symbols). The total average position error is slightly degraded from 33.2% to 34.7%. Fig. 5a shows for pixel 5 only, the theoretically calculated position error as a function of energy as well as the actual position error for 100 simulated pulses at 20, 50, 100 and 300 eV. In Fig. 5b we show, for the same data at 20, 50 and 100 eV, a histogram of the actual pixel assignments. Thus even if the pixel error is relatively high; the majority of incorrectly assigned events are assigned to the nearest neighbour pixels so the position resolution will not be completely lost. At 50 eV the average number of iterations (across all pixels) after the initial position estimate is 1.23, this falls to 1.12 at 100 eV and 1.02 at 300 eV. For the latter there is < 0.1 % position error across all pixels. Depending upon the number of absorber elements the number of iterations could be reduced by making an initial position estimate using some other measure such as rise-time for example.

At an energy of 50 eV, it was found that approximately 10 % of the total events, averaged over all absorbers, would fail to converge on a solution and iterated continuously between 2 pixels where in both cases $|\delta i| \geq 0.5$. In the implementation of the CEPOF we set the final pixel assignment to correspond to whichever pixel had the smallest $|\delta i|$. Of these events approximately 50 % were then correctly assigned. By rejecting these events some modest improvement in the total position error from 35 % to 33 % can be achieved, at the expense of a 10 % drop in throughput.

The term $F_i' S$ is a measure of the intrinsic correlation between energy and position and is required to give a self-consistent value of H and δi. In a continuous absorber PoST this energy-position correlation results in a degradation of the energy resolution and position resolution. In the segmented PoST, however, once we have converged on the correct pixel, the position-energy correlation disappears and this term can be dropped in calculating the photon

energy. Eq. 5b then reduces to the single pixel form of the energy resolution given by $\Delta E_i = (4\sum F_i S_i)^{-0.5}$. Fig. 6 shows the calculated FWHM energy resolution ($2.355\Delta E_i$) using the full CEPOF and that with the correlation term dropped. Thus dropping this term gives a more accurate estimate of the energy. At lower photon energies where we may have error in the position, then the resolution calculated using the full algorithm gives a better approximation to the actual energy resolution.

So far the analysis has assumed that the template responsivities and derivatives are calibrated in the small signal limit where the pulses are linear with energy. Assuming a higher calibration energy such as that from an ^{55}Fe source of 5.9 keV has the potential to introduce some level of non-linearity in the detector response. This has the potential to degrade the position sensitivity since the high energy template may not be well matched to the low energy linear pulse. The vast majority of non-linearity comes about from the dis-proportionality between the measured change in current ΔI and the TES resistance R ($\Delta I \propto 1/R^2$); this effect is intrinsically included in our model. The significance of this effect will depend upon the specific design parameters of the device in question. For our current Hydra example we find that by using the non-linear 5.9 keV template, we introduce no additional error in the position sensitivity though a small correction is required to re-calibrate the gain scale. At higher energies further non-linearity can occur due to the dependence of α and β on the resistive transition and saturation can occur when the TES is driven fully into the normal state. This effect does represent an extreme case and is neglected in our model since we keep α and β constant. If non-linearity effects are found to be a problem for a specific detector then using multiple calibration lines, or implementing non-linear optimal filtering techniques as discussed in ref [24] can be used to improve performance.

PoST's have an intrinsic trade-off between energy resolution and position sensitivity, which depends upon the ratio of the internal to external thermal conductances [16]. If the absorbers are all strongly thermally coupled to the TES, then the energy resolution will be optimal but there will be no signal variation with position. Reducing the internal conductances relative to the bath conductance introduces position dependence but attenuates the decoupled absorber signal relative to the noise (see Fig. 2), as well as adding more internal thermal noise. This is illustrated in Figs. 7 and 8 were we show the calculated FWHM energy resolution and position error respectively at 50 eV as a function

of the internal link conductances, which are normalised to the configuration described in Table 1. Only a subset of pixel data are shown. As the link conductances are reduced the position error passes through a minimum and then starts to degrade. This is because the degradation in signal-to-noise out-weighs any improvements due to increasing the separation of the pulse shapes. The minimum occurs at different conducatances for each pixel but are relatively broad, meaning it is possible to achieve both good position sensitivity and energy resolution across all absorber pixels. As the G_L's are reduced, the TES and most strongly coupled absorber become more and more isolated from the other elements and the energy resolution (without position correlation) improves. In the extreme limit of $G_L \rightarrow 0$ we find ΔE = 1.7 eV; since the energy resolution scales as the square root of the total heat capacity this is $\sqrt{9}$ times lower than the $G_L \rightarrow \infty$ case where ΔE = 5.1 eV.

5. Effect of random arrival phase

A potential difficulty with the implementation of the digital optimal filter on real data is that the measured signal is random in time and its correct phase relative to the filter is unknown. The variation in the arrival phase will depend upon the noise level relative to the signal and the shape of the initial pulse rise, as well as the method of triggering and the sample rate. Although calculated in the frequency domain, the optimal filter is usually applied as a cross-correlation in the time domain. If the phase of the filter and the pulse are the same then this will correctly give the photon energy (as well as position for the CEPOF). If the arrival phase is not known then the complete convolution over all phases is required. In the simple OF the peak in the convolution gives the correct arrival phase and photon energy with the lowest noise. Close to the maximum, phase errors give small errors in energy but if the phase error is large then the error in energy can become very much greater than the actual noise. Thus for discreetly sampled data it is typical to apply some phase correction algorithm, such as interpolating the energy between the quantised phase lags around the peak to more accurately measure the energy. Fig. 9a shows a plot of the convolution response as a function of phase lags for a 300 eV (noise free) pixel 1 pulse, calculated using both the CEPOF and the standard OF. Unlike the standard OF, the CEPOF convolution is asymmetric about zero lags and the peak cross-correlation does not give the optimum noise or the correct energy. This is the same as noted by Whitford (2005) [24] for similar non-linear (in energy) optimal filtering. The standard OF is sharply peaked around 0-lags because of the high frequency content in the filter and the pulse, and relatively small errors in lag could create a large error in energy. Fig. 9b shows the case for a pixel 8 pulse. For this slower pulse the dependence on lags is much less, so the potential

for error is smaller. Fig. 9c then shows δi for pixel 1 and 8 using the CEPOF. Since we only require $|\delta i| < 0.5$ for the correct pixel assignment, small phase shifts around the true phase do not result in any position error. If the jitter is greater than a few lags then some correction will be required. The fact that the peak in the convolution for the CEPOF does not correspond to the correct energy is an obvious problem for the implementation of the algorithm on random discretely sampled data. However, it is possible to correct for phase (at the level of integer lags) using the standard OF first and then, by applying the CEPOF we can converge on the final position. A final sub-lag phase correction (by interpolating between lags) using the standard OF can be used for the final estimation of the energy.

6. Summary and conclusions

We have demonstrated an implementation scheme for a correlated-energy-position optimal filter algorithm, which we have adapted for single-TES, segmented-absorber Hydras. Although in this paper we demonstrate the algorithm on Hydras devices, we have also implemented the algorithm on simulated 2-TES segmented PoST data with similar results. The CEPOF can be extended to include extra dimensions and any number of channels for segmented or continuous absorber devices. The CEPOF can also be implemented on other calorimeter technologies such as position-sensitive MMC's [18]. For a continuous device the CEPOF implementation will in principle be the same, however we have a continuous distribution of pulse shapes rather than a quantised set. The requirements on calibration are potentially higher for continuous devices, though could be reduced by interpolating the filter functions between a set of pre-computed calibration points at known x/L. The computational requirements of the CEPOF are only moderately more than the standard OF. Every absorber element whether in a single pixel array or a PoST array requires its own template filter. For the CEPOF we require the calculation of the additional normalisation constants (which only need to be calculated once) and the extra derivative filter convolution term. On the simulations reported here we on average required only one additional iteration of the CEPOF to converge on the correct position, hence the CEPOF is not likely to be significantly more computationally intense than the standard OF.

Acknowledgments

This research was in-part supported by appointment to the NASA Postdoctoral Program at Goddard Space Flight Center, administered by Oak Ridge Associated Universities through a contract with NASA. The author would like to

thank Caroline A. Kilbourne, Simon R. Bandler and Encetali Figueroa-Feliciano for many useful discussions in the preparation of this work.

References

[1] K.D. Irwin, G.C. Hilton, D.A. Wollman, J.M. Martinis, Appl. Phys. Lett. 69 (1995) 1945.

[2] A. Fleischmann, M. Link, T. Daniyaro, H. Rotzinger, C. Enss and G.M. Seidel, Nucl. Instr. and Meth. A 520 (2004) 27.

[3] J. Bookbinder, R. Smith, A. Hornschemeier, M. Garcia, N. White, H. Tananbaum, R. Petre, S. Romaine, P. Reid, Conf. Proc. SPIE, Space telescopes and instrumentation 2008: ultraviolet to gamma ray, vol. 7011, article 701102, 2008.

[4] A.N. Parmer, M. Arnaud, X. Barcons, J. Bleeker, G. Hasinger, H. Kunieda, G. Palumbo, T. Takahashi, M. Turner, P. de Korte, R. Willingale, N. Rando, A. Lyngvi, P. Gondonin, D. Lumb, M. Bavdaz, P. Verhoeve, Conf. Proc. SPIE, Space telescopes and instrumentation 2008: ultraviolet to gamma ray, vol. 6266, article 62661R, 2006.

[5] S.J. Wolk, R. J. Brissenden, M. Elvis, G. Fabbiano, A.E. Hornschemeier, S.L. O'Dell, M.W. Bautz, D.A. Schwartz, M. Juda, Conf. Proc. SPIE, Space telescopes and instrumentation 2008: ultraviolet to gamma ray, vol. 7011, article 701130, 2008.

[6] N. Iyomoto, S.R. Bandler, R.P. Brekosky, A.-D. Brown, J.A. Chervenak, F.M. Finkbeiner, R.L. Kelley, C.A. Kilbourne, F.S. Porter, J.E. Sadleir, S.J. Smith, E. Figueroa-Feliciano, Appl. Phys. Lett. 92 (2008) 013508.

[7] C.A. Kilbourne, W.B. Doriese, S.R. Bandler, R.P. Brekosky, A.-D. Brown, J.A. Chervenak, M.E. Eckart, F.M. Finkbeiner, G.C. Hilton, K.D. Irwin, N. Iyomoto, R.L. Kelley, F.S. Porter, C.D. Reintsema, S.J. Smith, J.N. Ullom, Conf. Proc. SPIE, Space telescopes and instrumentation 2008: ultraviolet to gamma ray, vol. 7011, article 701104, 2008.

[8] S.R. Bandler, A.-D. Brown, J. Chervenak, E. Figueroa-Feliciano, F. Finkbeiner, N. Iyomoto, R.L. Kelley, C. Kilbourne, F.S. Porter, S.J. Smith, J. Low Temp. Phys. 151 (2008) 400.

[9] E. Figueroa-Feliciano, PhD Thesis, Stanford University, 2001.

[10] N. Iyomoto, S.R. Bandler, R.P. Brekosky, J.A. Chervenak, E. Figueroa-Feliciano, F.M. Finkbeiner, R.L. Kelley, C.A. Kilbourne, M.A. Lindeman, K. Murphy, F.S. Porter, T. Saab, J.E. Sadleir, D.J. Talley, Nucl. Instr. and Meth. A 559 (2006) 491.

[11] S.J. Smith, C.H. Whitford, G.W. Fraser, D.J. Goldie, Nucl. Instr. and Meth. A 559 (2006) 500.

[12] R.A. Stern, A. Rausch, S. Deiker, D. Martínez-Galarce, L. Shing, K.D. Irwin, J.N. Ullom, G. O'Neil, G. Hilton, L. Vale, J. Low Temp. Phys. 151 (2008) 721.

[13] S.J. Smith, S.R. Bandler, R.P. Brekosky, A.-D. Brown, J.A. Chervenak, M.E. Eckart, F.M. Finkbeiner, R.L. Kelley, C.A. Kilbourne, F.S. Porter, E. Figueroa-Feliciano, Conf. Proc. SPIE, Space telescopes and instrumentation 2008: ultraviolet to gamma ray, vol. 7011, article 701126, 2008.

[14] S.J. Smith, S.R. Bandler, R.P. Brekosky, A.-D. Brown, J.A. Chervenak, M.E. Eckart, F.M. Finkbeiner, N. Iyomoto, R.L. Kelley, C.A. Kilbourne, F.S. Porter, J.E. Sadleir, E. Figueroa-Feliciano, Development of position-sensitive transition-edge sensor X-ray detectors, accepted for publication in IEEE Transaction on Applied Superconductivity (2008).

[15] S.J. Smith, S.R. Bandler, A.-D. Brown, J.A. Chervenak, E. Figueroa-Feliciano, F.M. Finkbeiner, N. Iyomoto, R.L. Kelley, C.A. Kilbourne F.S. Porter, J. Low Temp. Phys. 151 (2008) 1009.

[16] S.J. Smith, C.H. Whitford, G.W. Fraser, Nucl. Instr. and Meth. A, 556 (2006) 237-245.

[17] A.E. Szymkowiak, R.L. Kelley, S.H. Moseley, C.K. Stahle, J. Low Temp. Phys. 93 (1993) 281.

[18] S.J. Smith, JINST 2 (2007) P11005.

[19] W.H. Press, S.A. Teukolsky, W.T. Vetterling, B.P. Flannery, Numerical Recipes in C, 2nd edn., Cambridge University Press, Cambridge, 1995.

[20] K. D. Irwin, Nucl. Instr. and Meth. A. 559 (2006) 718.

[21] D. McCammon, Thermal Equilibrium Calorimeters – An Introduction, in Cryogenic Particle Detection, Topics in Applied Physics, vol. 99, Springer, ed. C. Enns, 2005.

[22] E. Figueroa-Feliciano, J. Appl. Phys. 99 (2006) 114513.

[23] S.J. Smith, PhD Thesis, University of Leicester, 2006.

[24] C.H. Whitford, Nucl. Instr. and Meth. A 555 (2005) 255–25.

Table 1. 9-Pixel Hydra model parameters. Note that absorber one is assumed infinitely well coupled to the TES.

Parameter	**Symbol and units**	**Value**
Heat capacity per absorber	C (pJ/K)	0.35
Thermal conductance to heat sink	G_b (pW/K)	650
TES transition temperature	T_c (mK)	90
Bath temperature	T_b (mK)	50
TES normal state resistance	R_N (mΩ)	7
Fractional bias point	R_0/R_N (%)	15
Bias circuit load resistor	R_l (mΩ)	0.25
Internal thermal conductances for absorbers 2-9	G_L (nW/K)	34, 21, 14, 10.3, 7.3, 5, 3.7, 3
TES resistance sensitivity	α	60
TES current sensitivity	β	2.0
SQUID input coil inductance	L_{in} (nH)	90
Integration step size	Δt (μs)	1.0
Number of samples per record	N_s	2^{15}

Figure captions

Fig. 1. (color online) Schematic diagram of the 9-pixel Hydra.

Fig. 2. a) (color online) Simulated 9-pixel Hydra noise-less pulse shapes for a photon energy of 100 eV. **b)** Power spectral density averaged from 400 simulated noise records and spectral density of the noise free pulse shapes.

Fig. 3. a) (color online) Calculated value for δi at each of the 9 Hydra absorber pixels for a 100 eV photon absorber at pixel $i = 5$. **b)** For the same example we show the calculated photon energy H using the complete algorithm and calculated assuming position and energy are independent.

Fig. 4. (color online) Theoretically calculated position error for each pixel at a photon energy of 50 eV. Also shown is the actual position error for a population of 100 simulated pulses assuming a starting position of $i = i_\gamma$ and then for the case $i = 5$.

Fig. 5. a) (color online) Theoretically calculated position error as a function of energy for pixel 5. Also shown is the actual position error for a population of 100 simulated pulses at energies of 20, 50, 100, 300 eV. **b)** Histogram of pixel assignments for simulated data at 20, 50 and 100 eV.

Fig. 6. (color online) FWHM energy resolution calculated using both the full CEPOF algorithm and dropping the energy-position correlation.

Fig. 7. (color online) FWHM energy resolution calculated using both the full CEPOF algorithm (solid lines) and dropping the energy-position correlation (dashed lines) as a function of the internal link thermal conductances G_L (G_L is normalized to configuration described in Table 1. Data is shown for pixels 1, 5 and 8.

Fig. 8. (color online) Position error at 50 eV as a function of normalized link conductance for pixels 1, 2, 5 and 8.

Fig. 9. a) (color online) Convolution of the CEPOF and standard OF with a 300eV pulse from pixel 1 as a function of phase lags. Zero lags corresponds to the correct arrival phase of the pulse relative to the filter. **b)** Same as for Fig. 9a using a pixel 8 pulse. **c)** δi for both pixel 1 and pixel 8.

Fig. 1.

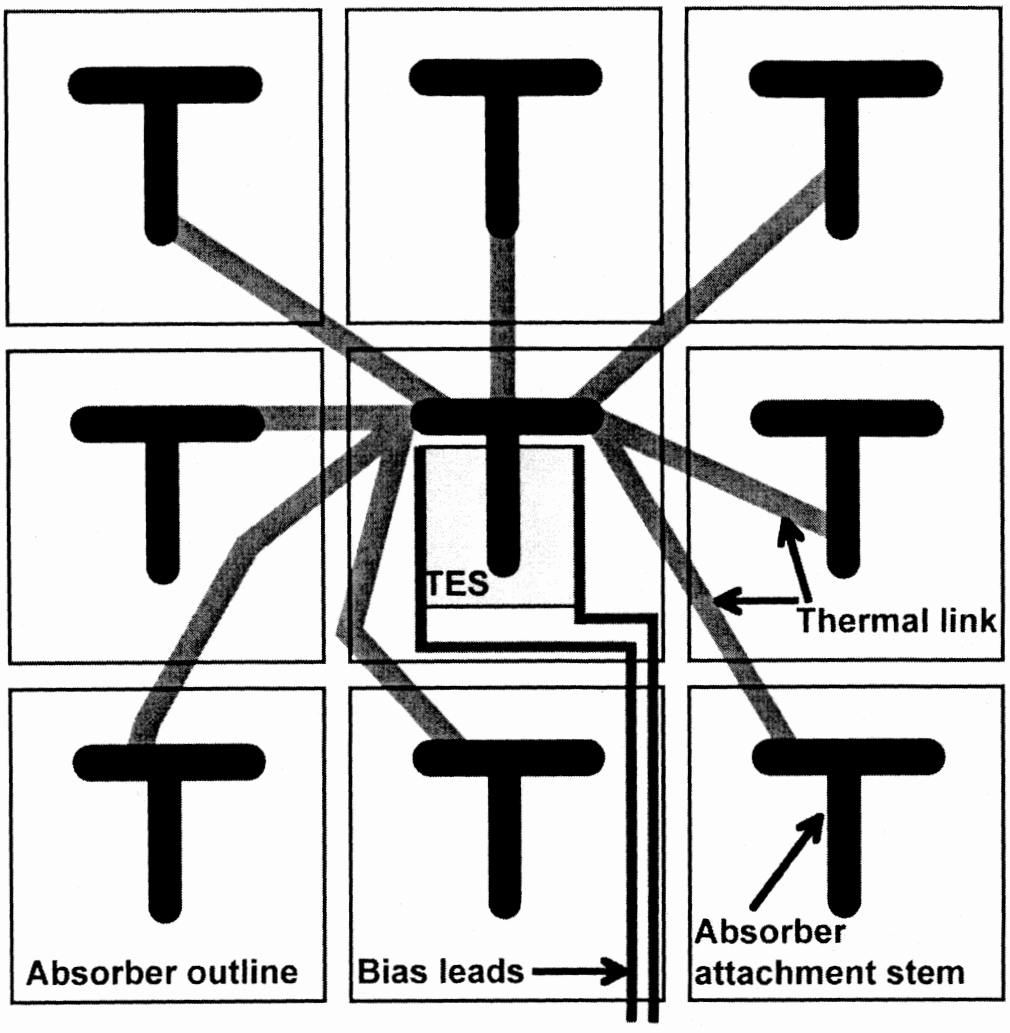
TES
Thermal link
Absorber outline
Bias leads
Absorber attachment stem

Fig. 2.

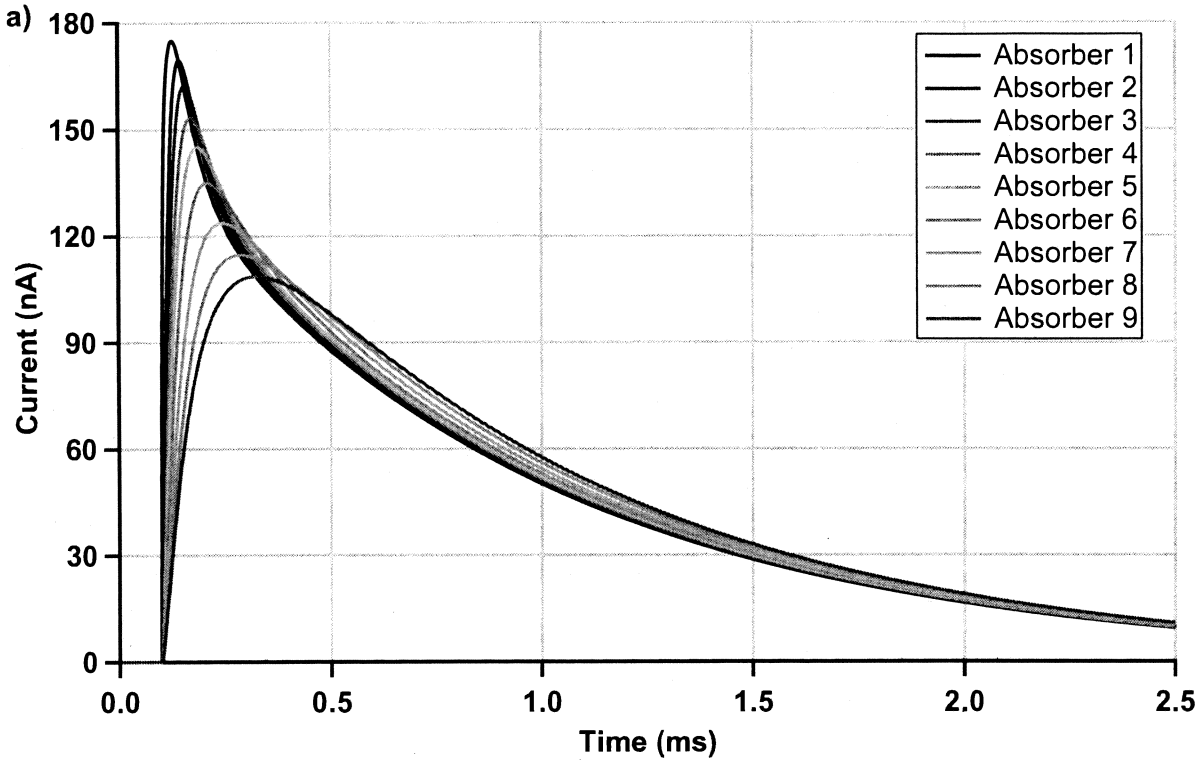
a)
Current (nA)
Time (ms)
Absorber 1
Absorber 2
Absorber 3
Absorber 4
Absorber 5
Absorber 6
Absorber 7
Absorber 8
Absorber 9

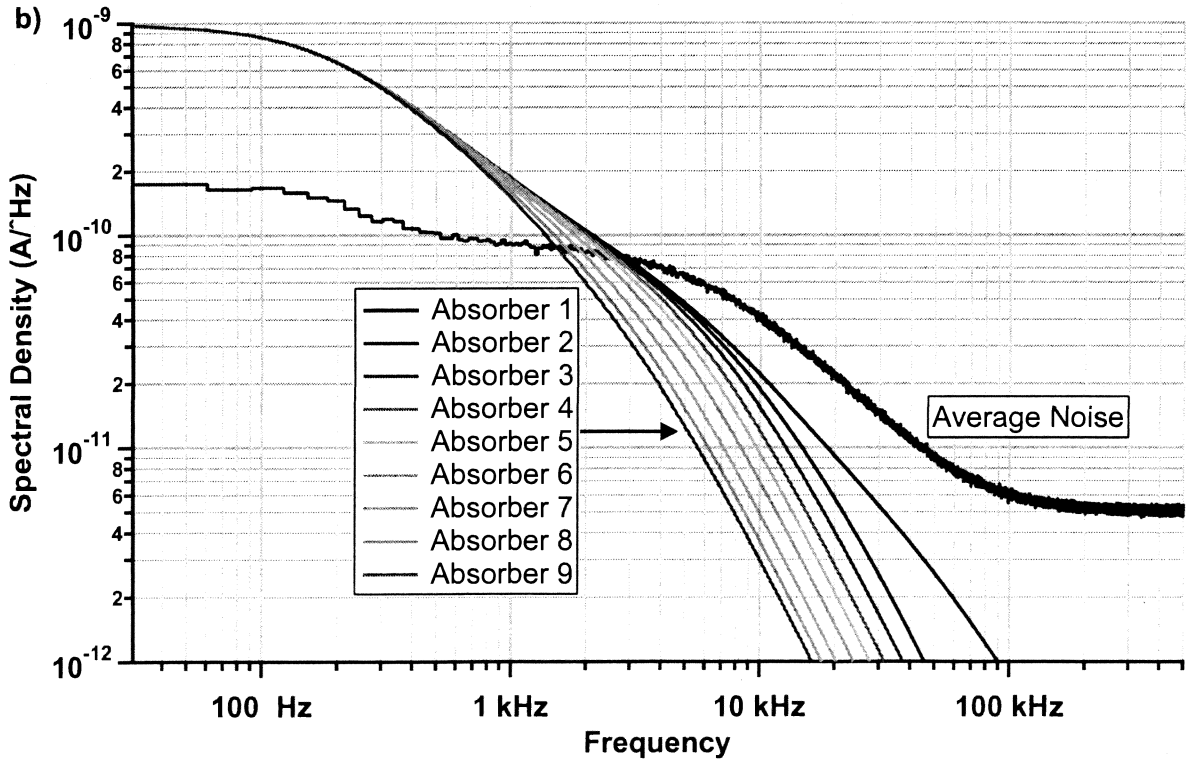
b)
Spectral Density (A/√Hz)
Frequency
100 Hz
1 kHz
10 kHz
100 kHz
Absorber 1
Absorber 2
Absorber 3
Absorber 4
Absorber 5
Absorber 6
Absorber 7
Absorber 8
Absorber 9
Average Noise

Fig. 3a,b.

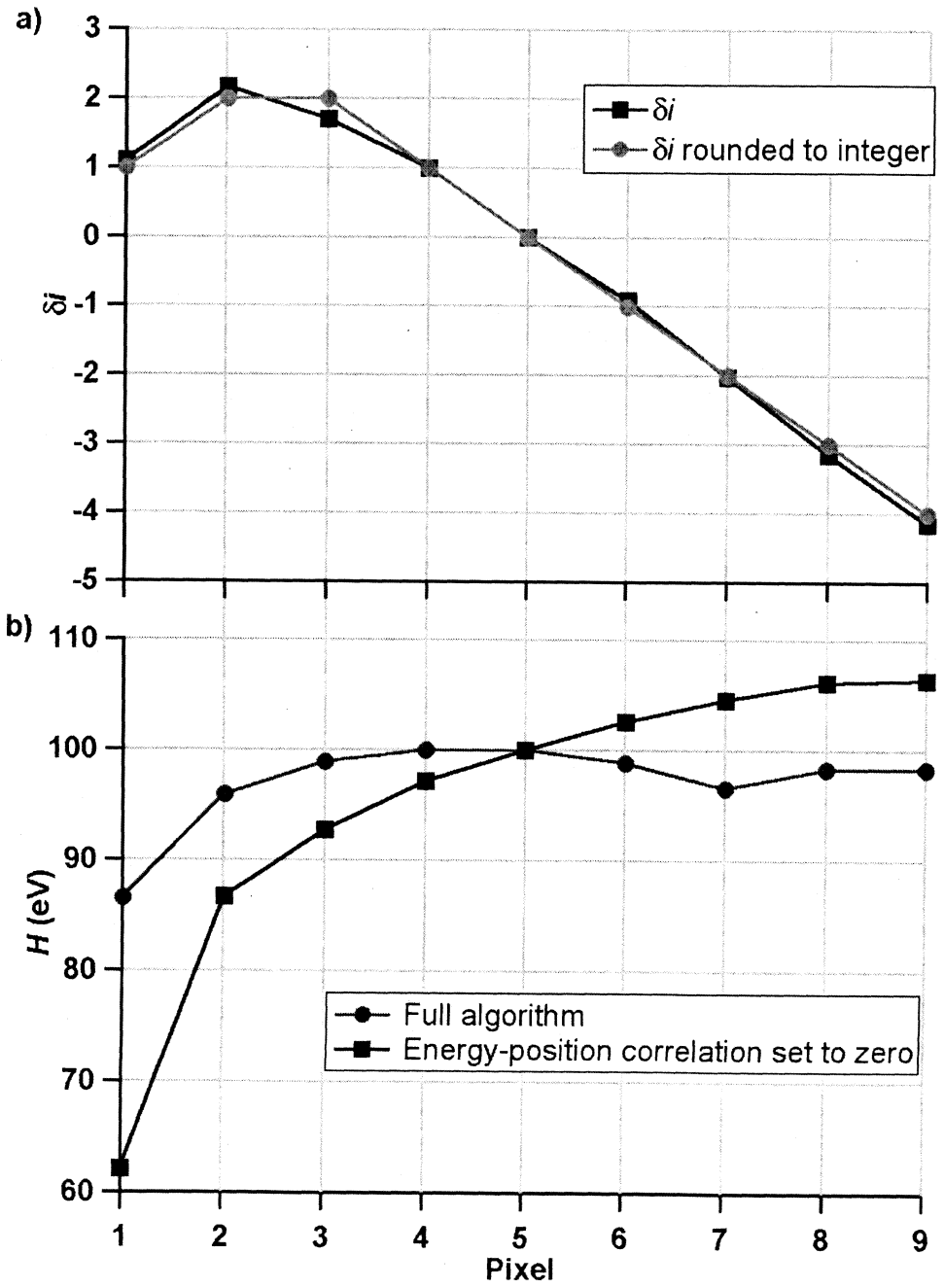
a)
δi
δi rounded to integer
b)
H (eV)
Full algorithm
Energy-position correlation set to zero
Pixel

Fig. 4.

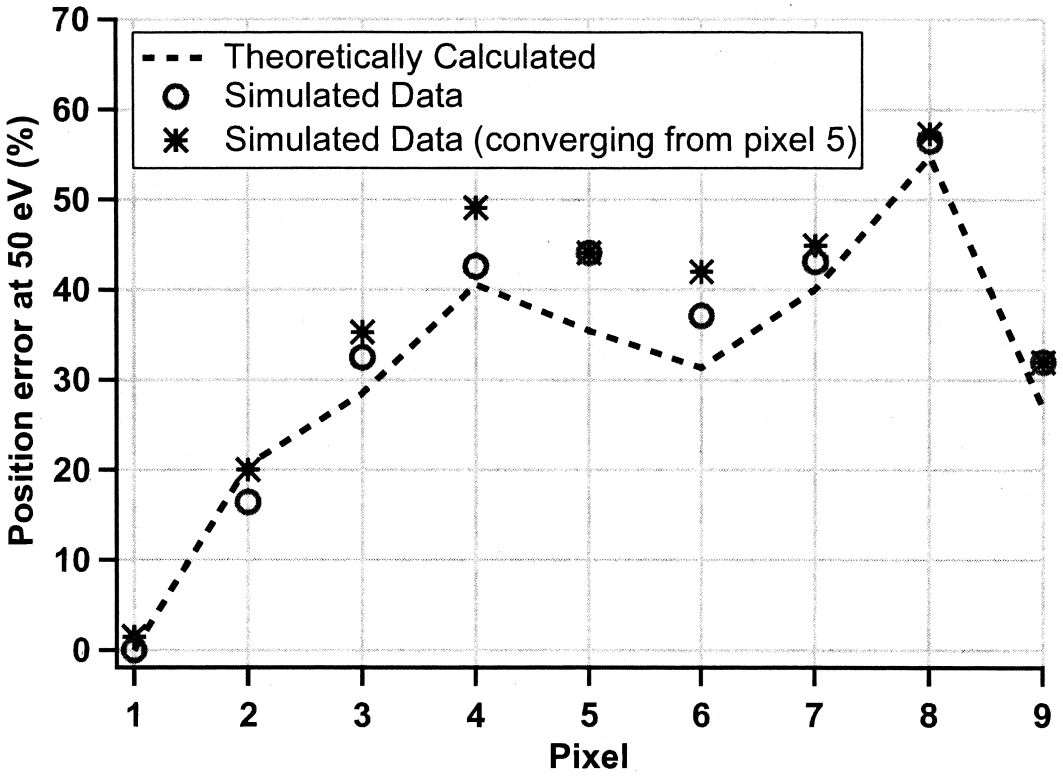
Theoretically Calculated
Simulated Data
Simulated Data (converging from pixel 5)
Position error at 50 eV (%)
Pixel
0
10
20
30
40
50
60
70
1
2
3
4
5
6
7
8
9

Fig. 5.

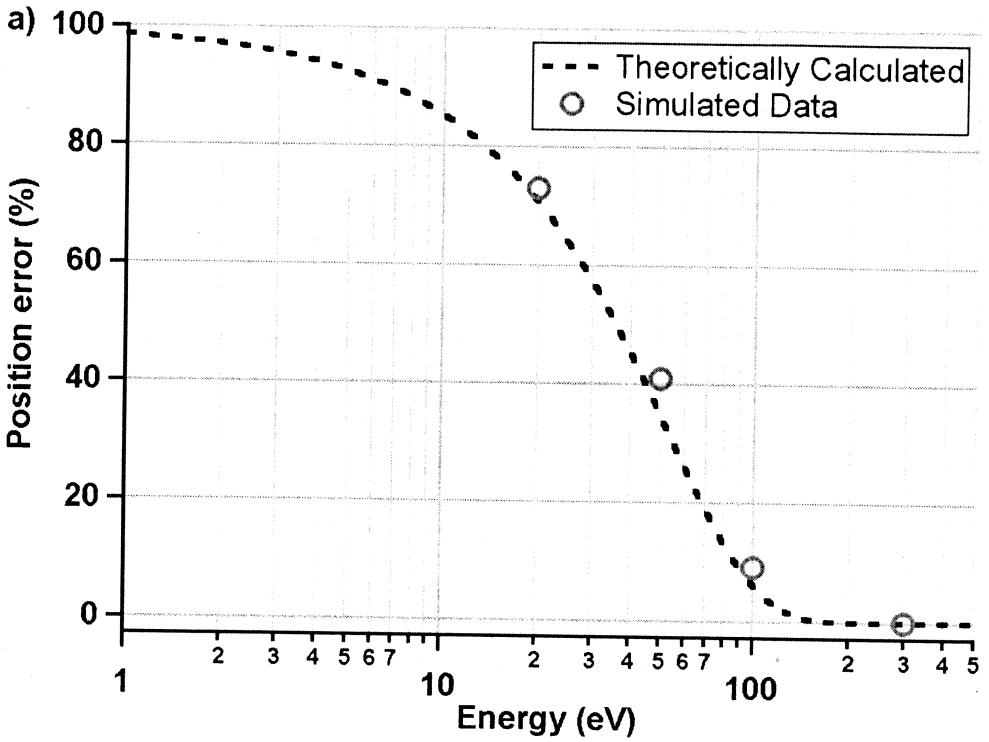
a)
Position error (%)
Energy (eV)
Theoretically Calculated
Simulated Data

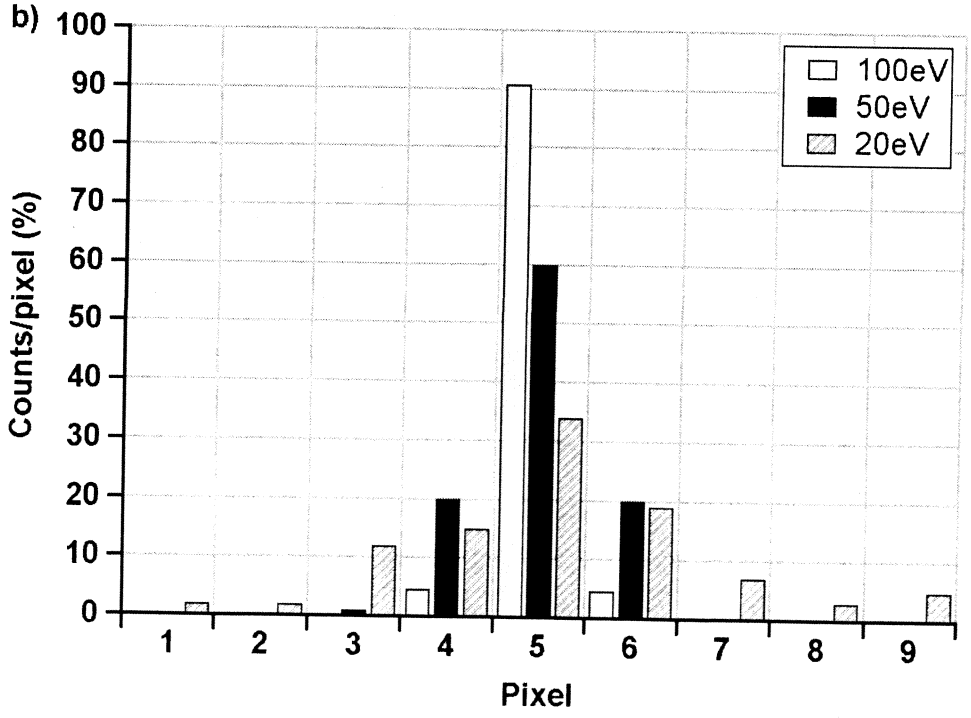
b)
Counts/pixel (%)
Pixel
100eV
50eV
20eV

Fig. 6.

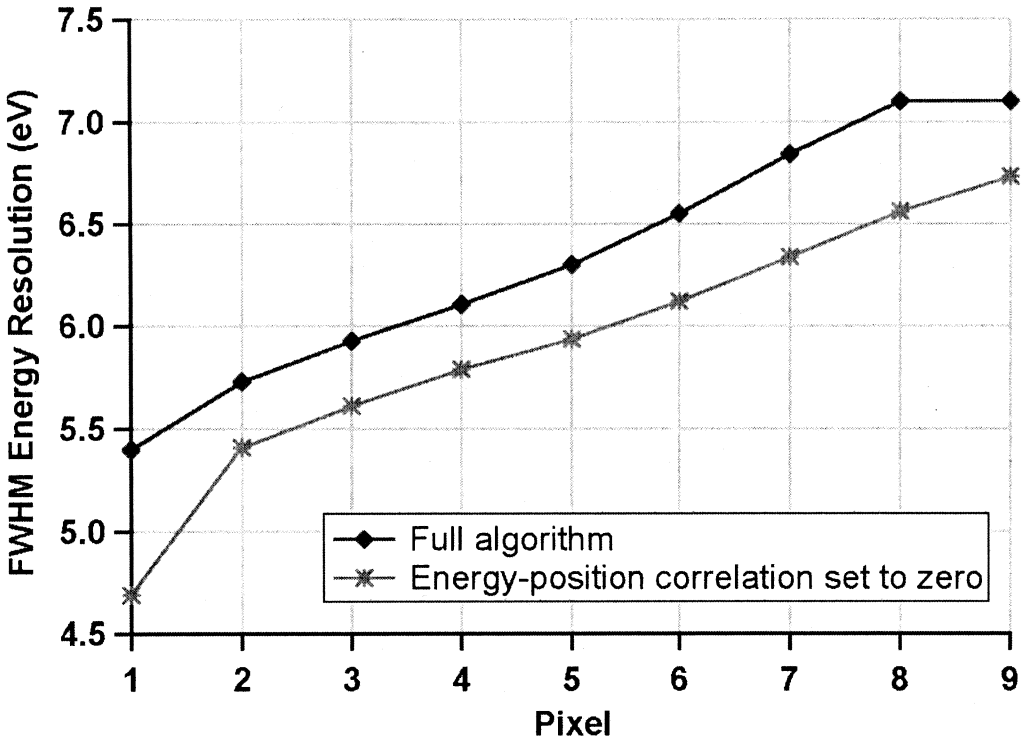
FWHM Energy Resolution (eV)
7.5
7.0
6.5
6.0
5.5
5.0
4.5
1
2
3
4
5
6
7
8
9
Pixel
Full algorithm
Energy-position correlation set to zero

Fig. 7.

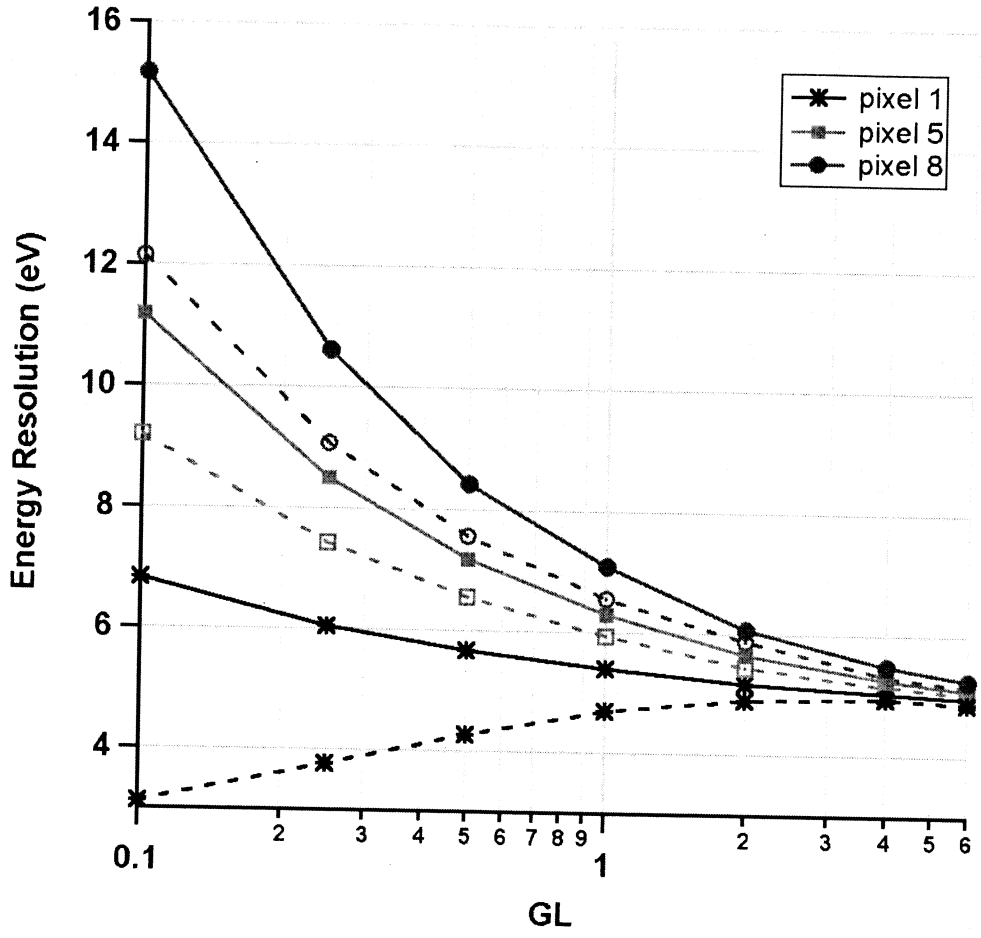
Energy Resolution (eV)
16
14
12
10
8
6
4
pixel 1
pixel 5
pixel 8
0.1
2
3
4
5
6
7
8
9
1
2
3
4
5
6
GL

Fig. 8.

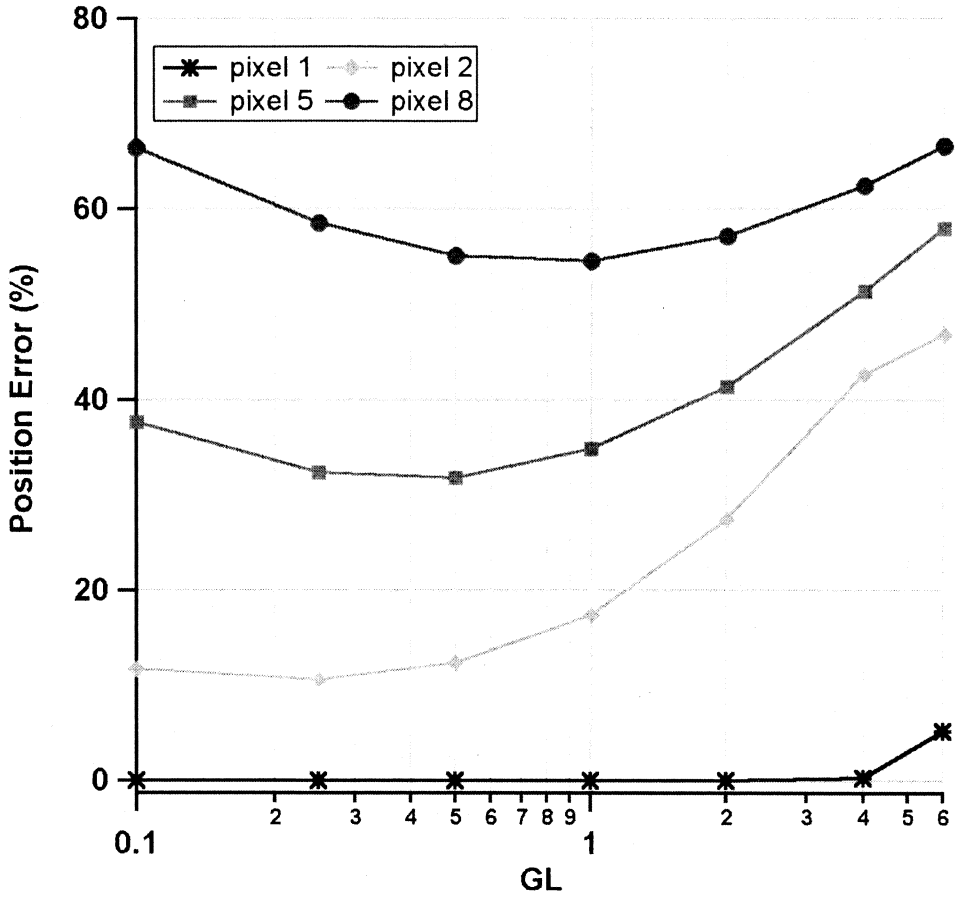
80
60
40
20
0
Position Error (%)
pixel 1
pixel 2
pixel 5
pixel 8
0.1
2
3
4
5
6
7
8
9
1
2
3
4
5
6
GL

Fig. 9.

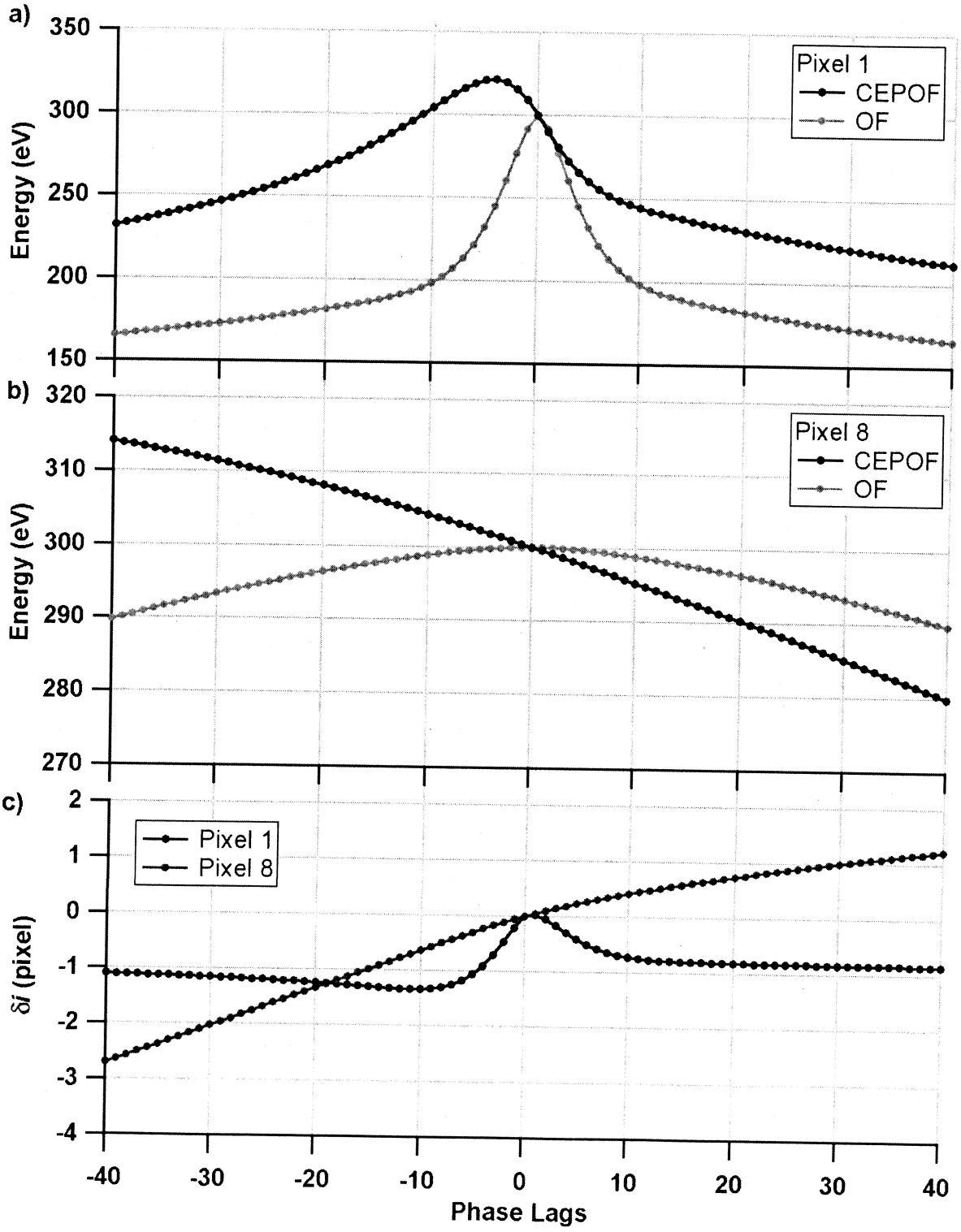
a)
Energy (eV)
Pixel 1
CEPOF
OF
b)
Energy (eV)
Pixel 8
CEPOF
OF
c)
Pixel 1
Pixel 8
δi (pixel)
Phase Lags